IEEE Access
Multidisciplinary | Rapid Review | Open Access Journal

Received 10 May 2023, accepted 19 June 2023, date of publication 22 June 2023, date of current version 27 June 2023.

Digital Object Identifier 10.1109/ACCESS.2023.3288832

RESEARCH ARTICLE

A Novel Multi-Hypothesis Filter for Terrain Aided Navigation

AYBARS TOKTA[1] AND ALİ KÖKSAL HOCAOĞLU[2]
[1]Aselsan Inc., Akyurt, 06750 Ankara, Turkey
[2]Department of Electronics Engineering, Gebze Technical University, 41400 Gebze/Kocaeli, Turkey
Corresponding author: Aybars Tokta (atokta@aselsan.com.tr)

This work was supported by Aselsan Inc.

ABSTRACT The susceptibility of GNSS signals has led to the development of advanced aiding systems in which information obtained from external sensors is fused with the inertial navigation solution to maintain navigation continuity in GNSS-denied environments. In terrain-aided navigation, the aim is to solve the horizontal position ambiguity of the platform with the help of pre-installed digital terrain elevation maps and estimated terrain height information obtained by the platform's barometer and distance measuring sensor readings. In this paper, we propose a novel multi-hypothesis terrain-aided navigation framework where horizontal position measurements are generated along with their covariance matrices from the estimated terrain heights. These measurements are fused with appropriate navigation hypotheses in a closed-loop configuration where augmented navigation error state estimates are fed into the navigation solution of the corresponding hypothesis. The number of hypotheses and their covariances change adaptively based on the terrain under the flight path preventing deviation from the true position for multi-modal or non-informative regions. The simulation results show that, unlike conventional TAN methods, the proposed method is able to yield accurate positioning estimations even when low-end IMUs are used. Furthermore, the proposed method is found to be effective in the presence of substantial initial errors in position, velocity, and heading.

INDEX TERMS Inertial navigation, terrain referenced positioning, terrain aided navigation.

I. INTRODUCTION

Inertial navigation systems (INS) have been around since the 40s. These systems contain an Inertial Measurement Unit (IMU) composed of an accelerometer and gyroscope triad to sense specific force and rotation with respect to the inertial frame. However, due to its integrating nature, systematic and stochastic errors in the IMU measurements cause degradation of position, velocity, and attitude (PVA). For this reason, high precision IMUs are usually employed in INS in critical platforms to ensure accurate PVA solutions [1]. Although these high-grade INS yield reasonable PVA accuracy, they are costly and large. To maintain an accurate PVA solution with affordable INS or for more prolonged durations, the Global Navigation Satellite System's (GNSS) low bandwidth and high accuracy position solution are integrated with INS output in almost every platform. However, GNSS signals are susceptible to jamming and spoofing and may be blocked or corrupted by obstructions [2]. Thus, information obtained from other sensors is fused with INS to limit the errors during GNSS outages. An aircraft is equipped with ranging sensors (radar or laser altimeter) to measure the distance underneath the aircraft (ground clearance distance) and a barometer to measure the height above the mean sea level (altitude). Terrain-aided navigation (TAN) is a type of navigation where the information obtained by the sensors mentioned previously, and Digital Terrain Elevation Data (DTED) are used to estimate the platform's position. In TAN, the terrain height profile beneath the aircraft path is calculated by subtracting ground clearance distance from the altitude reading. Then, the aircraft position is estimated using DTED and collected terrain height profile. There are two primary approaches in TAN literature: batch and recursive. A well-known batch TAN method is the terrain contour matching (TERCOM)

The associate editor coordinating the review of this manuscript and approving it for publication was Mohamed M. A. Moustafa.

algorithm [3], [4]. TERCOM estimates the current position by comparing the collected terrain height profile with the probable terrain heights evaluated from DTED at the horizontally shifted versions of the INS position output. The position shift that yields maximum similarity between the observed terrain height profile and calculated terrain height profile is regarded as a position error that is fed into the INS as a position fix. Sandia Inertial Terrain Aided Navigation (SITAN) [5] is the most famous approach among the recursive methods. In SITAN, terrain height error is predicted using gradients of the DTED map around the predicted navigation position. Then the difference between the measured terrain height error and this predicted terrain height error is used as an innovation in the Kalman filter correction step. There are several studies inspired by the TERCOM and SITAN architectures. In [6], TERCOM is utilized along with a particle filter to estimate the initial position under high uncertainty. Sonmez and Bingol demonstrate the effectiveness of TERCOM in land vehicles [7]. In [8], a probabilistic data association filter is employed to convert TERCOM correlation scores to probability values. Peng proposes a two-stage matching algorithm involving coarse terrain-based matching followed by contour-based fine matching [9]. There are some studies in which TERCOM and SITAN solutions are fused to increase robustness [10], [11], [12], [13].

There are also numerous non-linear estimation-based methods in the TAN literature. Enns and Morrell proposed a maximum a posteriori (MAP) based method [14]. Bergman et al. address the TAN problem in a bayesian framework where a point mass filter is utilized [15], [16]. Apparently, the particle filter (PF) approach to the TAN problem is first mentioned in [17]. Turan and Kutay test the performance of two different PF resampling methods in TAN [18]. Rao-Blackwellized implementations of PF, in which the linear and non-linear parts of the state vector are separated, have been extensively utilized in recent studies related to Terrain-Aided Navigation for underwater vehicles [19], [20], [21]. Rupeng et al. proposes a terrain aided positioning (TAP) confidence interval model for PF to mitigate the initial TAN positioning error [22]. In [23], estimation performances of PF and Unscented Kalman Filter (UKF) are compared. Ignoring the PVA error dynamics in INS, the studies mentioned so far employ a fairly simple process model to represent the dynamic of the platform state in which some IMU error sources, particularly accelerometer and gyroscope biases effects, are modeled as process noise. Such modeling simplification disregards the realistic error growth contributed by various IMU error sources in PVA states, which probably leads to a model mismatch in real-time applications, especially when low to mid-end IMUs are used [24]. Nordlund and Gustafsson propose a marginalized particle filter-based method where the linearized INS error propagation model is utilized in PF-based TAN for the first time [25]. Although PFs are widely used in non-linear estimation problems, as particles can represent any distribution, they also possess some issues. First, PF algorithms become computationally demanding as the number of states increases [26]. Second, Particle Filter solutions may diverge when the posterior distribution is multi-modal, which can frequently arise in Terrain-Aided Navigation problems due to topographical symmetries. These symmetries are characterized by shapes and structures in the region that exhibit similar heights, making it challenging to distinguish between different possible locations. This divergence issue in the TAN problem has been investigated in some studies. Palmier et al. introduced the Interacting Weighted Ensemble Kalman Filter (IWEnKF), which reduces the probability of divergence [27]. Likewise, Teixeira et al. proposed some ad-hoc methods to address the divergence issue in PFs for underwater TAN problems [28]. However, these approaches utilize a relatively simplistic motion model to represent the vehicle's dynamics, and do not account for numerous IMU error sources. In this study, we propose a novel TAN method in which we generate multiple horizontal position measurements and their covariance matrices which are then governed in a multi-hypothesis structure. The proposed structure accomplishes rapid convergence while also maintaining robustness against divergence as the platform flies over flat or multi-modal areas. We test the effectiveness of our method in a challenging simulation setup where initial PVA errors are significant. We also use low-end IMU specs during the synthetic data generation. The rest of the paper is organized as follows. The problem formulation, used notation, and motivation are provided in Section II. We discuss the mathematical details of the proposed method in Section III. In Section IV, we present the simulation results. The conclusion and future works are presented in Section V. In the Appendix, we emphasize some basic concepts related to INS.

II. NOTATION AND MOTIVATION

Before we explain the proposed TAN method in greater detail, we introduce the notation we use in this work. The notation related to the inertial navigation is as follows. The geodetic position vector $\mathbf{p} \triangleq [l\ L\ h]^T$ is composed of latitude(l), longitude(L), and altitude(h). The vector $\mathbf{v}^N \triangleq [v_n\ v_e\ v_d\ ]^T$ represents the velocity vector of the platform resolved in the North-East-Down (NED) frame. The attitude of the body with respect to NED frame is expressed by the Euler angle vector $\boldsymbol{\psi} \triangleq \left[\epsilon_r\ \epsilon_p\ \epsilon_y\right]^T$ which is composed of roll(ϵ_r), pitch(ϵ_p), and yaw (or heading)(ϵ_y) angles in radians. The gyroscope and accelerometer output of the IMU at time t are denoted by $\boldsymbol{\omega}^B_{\mathrm{IB}}(t)$ and $\boldsymbol{f}^B_{\mathrm{IB}}(t)$, respectively. In inertial navigation, the PVA error dynamics equation is derived by perturbating the mechanization equations around the nominal PVA solution. The obtained error dynamics equation is in the linear form, enabling it to be used as process model in the Kalman filter. Thus, in INS-related fusion problems, the errors in PVA are set as states to be estimated dynamically rather than the actual PVA values [1], [29], [30]. In this work, we use the augmented error state model [31] where IMU-related error parameters are included in the state vector. So, the augmented state vector to be estimated is composed

of position error $\delta\mathbf{p} \triangleq [\delta l\ \delta L\ \delta h]^T$, velocity error $\delta\mathbf{v}^N \triangleq [\delta v_n\ \delta v_e\ \delta v_d\ ]^T$, attitude error $\delta\boldsymbol{\psi} \triangleq \left[\delta\epsilon_r\ \delta\epsilon_p\ \delta\epsilon_y\right]^T$ gyroscope scale factor error $\delta\boldsymbol{\omega}_{\mathrm{SF}}$, misalignment error $\delta\boldsymbol{\omega}_{\mathrm{MA}}$, bias repeatability error $\delta\boldsymbol{\omega}_{\mathrm{BR}}$, bias instability error $\delta\boldsymbol{\omega}_{\mathrm{BI}}$ and, accelerometer counterparts of the same errors: $\delta\boldsymbol{f}_{\mathrm{SF}}$, $\delta\boldsymbol{f}_{\mathrm{MA}}$, $\delta\boldsymbol{f}_{\mathrm{BR}}$, $\delta\boldsymbol{f}_{\mathrm{BI}}$. Each of these IMU errors is 3×1 vectors (except for misalignment error that is 6×1 vector) whose elements indicate the corresponding error on the body X,Y, and Z axes, respectively. Manufacturers often share the standard deviation of these IMU error terms, or these statistics can be estimated via various techniques such as Allan-variance [24], [32], [33]. We briefly mention the inertial navigation mechanization equations, error dynamics equations, and IMU error parameters in the Appendix. We define the (augmented) error state as given in (1)

$$\delta\boldsymbol{X} \triangleq \begin{bmatrix}\delta\boldsymbol{X}_{\mathrm{PVA}}\\ \delta\boldsymbol{X}_{\mathrm{IMU}}\end{bmatrix}_{39\times1} \tag{1}$$

where;

$$\delta\boldsymbol{X}_{\mathrm{PVA}} \triangleq \left[\delta\boldsymbol{\psi}^T\ \ \delta\mathbf{v}^T\ \ \delta\mathbf{p}^T\right]^T_{9\times1} \tag{2}$$

$$\delta\boldsymbol{X}_{\mathrm{IMU}} \triangleq \left[\delta\boldsymbol{X}^T_{\mathrm{GYRO}}\ \ \ \delta\boldsymbol{X}^T_{\mathrm{ACCEL}}\right]^T_{30\times1} \tag{3}$$

where;

$$\delta\boldsymbol{X}_{\mathrm{GYRO}} \triangleq \left[\delta\boldsymbol{\omega}^T_{\mathrm{SF}}\ \ \delta\boldsymbol{\omega}^T_{\mathrm{MA}}\ \ \delta\boldsymbol{\omega}^T_{\mathrm{BR}}\ \ \delta\boldsymbol{\omega}^T_{\mathrm{BI}}\right]^T_{15\times1} \tag{4}$$

$$\delta\boldsymbol{X}_{\mathrm{ACCEL}} \triangleq \left[\delta\boldsymbol{f}^T_{\mathrm{SF}}\ \ \delta\boldsymbol{f}^T_{\mathrm{MA}}\ \ \delta\boldsymbol{f}^T_{\mathrm{BR}}\ \ \delta\boldsymbol{f}^T_{\mathrm{BI}}\right]^T_{15\times1} \tag{5}$$

The conditional error state vector and it's covariance matrix are defined as given in (6) and (7)

$$\widehat{\delta\boldsymbol{X}}(t_i|t_j) \triangleq E[\delta\boldsymbol{X}(t_i)|\delta\boldsymbol{z}^{t_0:t_j}] \tag{6}$$

$$P(t_i|t_j) \triangleq E\left([\widehat{\delta\boldsymbol{X}}(t_i|t_j)-\delta\boldsymbol{X}(t_i)][\widehat{\delta\boldsymbol{X}}(t_i|t_j)-\delta\boldsymbol{X}(t_i)]^T\ \ |\delta\boldsymbol{z}^{t_0:t_j}\right) \tag{7}$$

In the above equations, $\delta\boldsymbol{z}^{t_0:t_j}$ denotes the set of observed position errors from time t_0 up to t_j. The cases of $t_i = t_j$ and $t_i > t_j$ correspond to *estimated* and *predicted* states and state covariance matrices, respectively. For the sake of brevity, we use the superscripts $^+$ and $^-$ to indicate estimated and predicted states or covariance matrices for the rest of the paper. The dynamics of the true error state can be represented in the linear state-space form as given in (8)

$$\dot{\delta\boldsymbol{X}}(t) = F(t)\delta\boldsymbol{X} + G(t)\mathbf{w}(t) \tag{8}$$

where $F(t)_{39\times39}$ is the state transition matrix, $\mathbf{w}(t)_{12\times1}$ is a random input vector whose elements are standard normal random variables representing the white noise terms such as velocity and random walk specifications of the IMU and $G(t)_{39\times12}$ is the noise gain matrix. We discuss the details related to $F(t)$, $G(t)$, and $\mathbf{w}(t)$ in the Appendix. Similarly, the measurement equation can be represented as follows:

$$\delta\boldsymbol{z}(t) = H\delta\boldsymbol{X}(t) + \boldsymbol{v}(t) \tag{9}$$

where $H_{3\times39}$ is the measurement matrix and $\boldsymbol{v}(t)_{3\times1}$ is the Gaussian white noise vector representing the uncertainty in the measured position error. The equations (8) and (9) are linear, and noise terms $\boldsymbol{w}(t), \boldsymbol{v}(t)$ are modeled as zero-mean Gaussian independent of each other $\left(E[\boldsymbol{w}(t_k)\boldsymbol{v}(t_j)] = 0 \quad \forall(t_i, t_j)\right)$ with the covariance matrices $Q(t)$ and $R(t)$, respectively. Thus, utilizing the Kalman filter to recursively estimate $\widehat{\delta\boldsymbol{X}}$ and its covariance matrix P is a standard routine in INS-related fusion problems. For example, in loosely-coupled INS-GNSS integration, $\delta\boldsymbol{z}(t)$ is constructed by subtracting the lever-arm compensated geodetic position output of the GNSS receiver from the INS geodetic position [34]. Observing the position error makes all of the $\delta\boldsymbol{X}_{PVA}$ state components, along with some part of the $\delta\boldsymbol{X}_{\mathrm{GYRO}}$, and $\delta\boldsymbol{X}_{\mathrm{ACCEL}}$ observable as the platform maneuvers [35], [36]. However, in TAN, terrain height measurement beneath the platform does not give direct information about the platform's horizontal position (latitude, longitude). Correlation-based approaches like TERCOM resolves this horizontal position ambiguity by comparing the collected terrain height profile with DTED. But, correlation-based approaches assume that the position errors during terrain height acquisition remain fixed. Deploying tactical or sub-tactical grade IMU or having a velocity error at the beginning of the acquisition mode causes the accumulation of cross-track errors at the end of the mode, which degrades the accuracy of the position error estimation of correlation-based methods [37]. Linearized Kalman filter-based approaches like SITAN resolve the horizontal position ambiguity by deploying terrain slope information around the position estimate in the measurement model. However, this linearization process is highly sensitive to terrain shape and leads to incorrect estimates when the initial position uncertainty is significant [10]. The primary motivation of our study is to develop a TAN method that is robust to substantial initial PVA errors and yields reasonable performance even when low-end IMUs are used.

III. MULTI-HYPOTHESIS STRUCTURE IN TAN

Hypotheses constitute the core part of the proposed method. The main components of the method are demonstrated in Fig. 1 where a loop that starts and ends in hypothesis set propagation corresponds to a single cycle of the algorithm. Between the terrain aid cycles, hypotheses are propagated using IMU and barometer measurements. During the terrain aid cycles, multiple horizontal measurements and their covariance matrices are generated from the statistics of the clustered probable locations obtained from hypotheses. These probable locations are unique for each hypothesis and correspond to the locations within a certain percentage of the hypothesis horizontal uncertainty region that have similar heights obtained from DTED and measured terrain height using altimeter sensor readings. Once the horizontal measurements are generated, they are associated and fused with appropriate hypotheses. Similar hypotheses are merged, and unlikely hypotheses are pruned to limit the computational

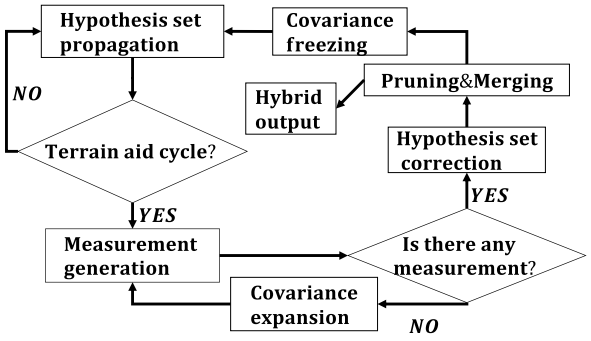

FIGURE 1. Flowchart of the proposed TAN algorithm.

burden. We also propose additional covariance manipulations to prevent divergence for long TAN durations. In the following part of the paper, we discuss the details of each flowchart component in greater detail.

A. THE DEFINITION OF HYPOTHESIS AND MULTI-HYPOTHESIS

A hypothesis can be considered as an independent INS system with its own navigation properties, error state, and error state covariance matrix. Individual Kalman filters that run parallel estimate the error state of each hypothesis at every terrain aid cycle if they are assigned a suitable measurement. We denote ξ symbol to represent a hypothesis and $\beta^{\xi_i}(t)$ to imply the β feature of the hypothesis ξ_i at time t. β can take any PVA property, error state or error state covariance mentioned in Section-II. Thus, β can take any symbol in the set $\left\{\hat{\boldsymbol{p}}, \hat{\boldsymbol{v}}, \hat{\boldsymbol{\psi}}, \delta\hat{\boldsymbol{X}}, P\right\}$ If there is a subscript of β, that means only the elements indicated by the subscript is implied. For example, $\hat{\boldsymbol{p}}^{\xi_i}(t)$ corresponds to 3×1 geodetic position vector that is $[l\ L\ h]^T$ of the hypothesis ξ_i at time t whereas $\hat{\boldsymbol{p}}^{\xi_i}_{l,L}(t)$ represents the 2×1 vector containing only the horizontal components of the geodetic position vector that is $[l\ L]^T$. Similarly, $\delta\hat{\boldsymbol{X}}^{\xi_i}(t)$ represents the whole 39×1 error state of the hypothesis ξ_i at time t whereas $\delta\hat{\boldsymbol{X}}^{\xi_i}_{\mathrm{v_N},\mathrm{v_E}}(t)$ represents 2×1 error state vector containing only the north and east velocity errors of the hypothesis ξ_i at time t. On the other hand, a multi-hypothesis, denoted by $\Xi(t)$, corresponds to a collection of hypotheses at time t, such as $\{\xi_1, \xi_2, \ldots, \xi_n\}$ where ξ_i for $i = 1, 2, \ldots, n$ represents individual hypotheses at time t.

B. HYPOTHESIS SET PROPAGATION

Let's assume that ground clearance distance measurements (obtained by a distance measuring device such as radar/laser altimeter) are fused with INS at times $t_{Ra(k)}$ for $k \in \{1, 2, \ldots, K\}$ where $t_{Ra(k)}$ denotes k^{th} terrain aid cycle time. Let Δt_{IMU} and T_{IMU} denote the time difference between two successive IMU measurements and the set of times when IMU measurements are received, respectively. The hypothesis propagation step occurs during the time frames $T_{\mathrm{Pr}}(k)$ for $k \in \{1, 2, \ldots, , K\}$ where $T_{\mathrm{Pr}}(k)$, as defined in (10), corresponds to the set of IMU times between two terrain aid cycles at time $t_{Ra(k-1)}$ and $t_{Ra(k)}$.

$$T_{\mathrm{Pr}}(k) \triangleq \left\{t \mid t_{Ra(k-1)} < t \leq t_{Ra(k)}, t \in T_{\mathrm{IMU}}\right\} \tag{10}$$

The term *hypothesis set propagation* refers to updating all properties of hypotheses between two terrain aid cycles. To perform this propagation, PVA, error state, and error covariance property of each hypothesis in the set $\Xi^+\left(t_{Ra(k-1)}\right)$ are propagated using the set of IMU and barometer measurements from time $t_{Ra(k-1)}$ to $t_{Ra(k)}$, that is $\left\{\boldsymbol{\omega}^B_{\mathrm{IB}}(t), \boldsymbol{f}^{\mathrm{B}}(t), h_{\mathrm{B}}(t) \mid t \in T_{\mathrm{Pr}}(k)\right\}$. The obtained hypotheses at the end of the cycle form the predicted hypothesis set $\Xi^-\left(t_{Ra(k)}\right)$. The hypothesis set propagation follows the procedure given in Algorithm 1. In this algorithm, $\hat{\boldsymbol{X}}^{\xi}_{\mathrm{PVA}}$ is the PVA vector consisting of attitude ($\hat{\boldsymbol{\psi}}^{\xi}$), velocity ($\hat{\boldsymbol{v}}^{\xi}$), position ($\hat{\boldsymbol{p}}^{\xi}$) vectors of the hypothesis ξ. $\delta\hat{\boldsymbol{X}}^{\xi}$ and P^{ξ} are the error state and the error state covariance matrix of the hypothesis ξ, respectively. In line 4, the raw IMU measurements are corrected using each hypothesis's estimated IMU error states from the previous terrain aid cycle. In lines 5, 6, and 7, the attitude, velocity, and position of the individual hypotheses are updated using discrete INS mechanization equations [38], [39]. In line 8, a baro-inertial vertical channel filter is performed [29]. We do not delve into the mechanization equations here to avoid veering off the main topic. In lines 9 and 10, Kalman filter error state and error state covariance matrix propagation are performed, where $\Phi(t)$ and $Q_d(t)$ are the discrete state transition and process noise covariance matrices. These matrices are obtained by discretizing their continuous counterparts, $F(t)$ and $Q(t)$, using Van Loan's method [40].

Algorithm 1 Hypothesis Set Propagation

Input: $\Xi^+\left(t_{Ra(k-1)}\right), \left\{\boldsymbol{\omega}^{\mathrm{B}}_{\mathrm{IB}}(t), \boldsymbol{f}^{\mathrm{B}}(t), h_{\mathrm{B}}(t) \mid t \in T_{\mathrm{Pr}}(k)\right\}$
Output: $\Xi^-\left(t_{Ra(k)}\right)$

1: $\Xi^-\left(t_{Ra(k)}\right) = \emptyset$
2: **for** each $\xi \in \Xi^+\left(t_{Ra(k-1)}\right)$ **do**
3: **for** each $t \in T_{\mathrm{Pr}}(k)$ **do**
4: $[\bar{\boldsymbol{\omega}}^{\mathrm{B}}_{\mathrm{IB}}, \bar{\boldsymbol{f}}^{\mathrm{B}}] = correctIMU(\boldsymbol{\omega}^{B}_{\mathrm{IB}}(t), \boldsymbol{f}^{\mathrm{B}}(t), \delta\hat{\boldsymbol{X}}^{\xi}_{\mathrm{IMU}})$
5: $\hat{\boldsymbol{X}}^{\xi}_{\mathrm{PVA}} = updateAttitude(\hat{\boldsymbol{X}}^{\xi}_{\mathrm{PVA}}, \bar{\boldsymbol{\omega}}^{\mathrm{B}}_{\mathrm{IB}})$
6: $\hat{\boldsymbol{X}}^{\xi}_{\mathrm{PVA}} = updateVelocity(\hat{\boldsymbol{X}}^{\xi}_{\mathrm{PVA}}, \bar{\boldsymbol{f}}^{\mathrm{B}})$
7: $\hat{\boldsymbol{X}}^{\xi}_{\mathrm{PVA}} = updatePosition(\hat{\boldsymbol{X}}^{\xi}_{\mathrm{PVA}})$
8: $\hat{\boldsymbol{X}}^{\xi}_{\mathrm{PVA}} = stabilizeVerticalChannel(\hat{\boldsymbol{X}}^{\xi}_{\mathrm{PVA}}, h_{\mathrm{B}}(t))$
9: $\delta\hat{\boldsymbol{X}}^{\xi} = \Phi(t)\,\delta\hat{\boldsymbol{X}}^{\xi}$
10: $P^{\xi} = \Phi(t)\,P^{\xi}\,\Phi(t)^T + Q_d(t)$
11: **end for**
12: append ξ into $\Xi^-\left(t_{Ra(k)}\right)$
13: **end for**

C. MEASUREMENT GENERATION

The measurement generation step takes place at the beginning of every terrain aid cycle. The purpose of this step is to generate horizontal measurements, along with their corresponding

covariance matrices within the uncertainty regions of available hypotheses, using the collected altimeter measurements and DTED map. Let $h_{Ter}(\boldsymbol{p}_{l,L})$, $h_{Bar}(\boldsymbol{p})$, and $h_{Ra}(\boldsymbol{p})$ denote the true terrain height, measured barometric altitude, and the measured ground clearance distance at the geodetic position $\boldsymbol{p} = [l\ L\ h]^T$. Then, we can express the true terrain height of any arbitrary 2D horizontal location $\boldsymbol{p}_{l,L}$ as given in (11).

$$h_{Ter}(\boldsymbol{p}_{l,L}) = (h_{Bar}(\boldsymbol{p}) - \Delta_{Bar}) - (h_{Ra}(\boldsymbol{p}) - \Delta_{Ra}) \tag{11}$$

where Δ_{Bar} and Δ_{Ra} are the pressure altimeter and radar(or laser) altimeter errors. Similarly, the relation between true terrain height and the calculated terrain height via DTED map at $\boldsymbol{p}_{l,L}$ can be established as given in (12).

$$h_{Ter}(\boldsymbol{p}_{l,L}) = \mathcal{H}(\boldsymbol{p}_{l,L}) - \Delta_{Dted} \tag{12}$$

where $\mathcal{H}(\boldsymbol{p}_{l,L})$ is the DTED referenced terrain height calculated by the bilinear interpolation method using four adjacent grid heights of the horizontal position $\boldsymbol{p}_{l,L}$ and Δ_{Dted} corresponds to the DTED error at the point $\boldsymbol{p}_{l,L}$. Assuming the error terms in (11) and (12) are independent zero-mean Gaussians with the variances $\sigma^2_{Bar}, \sigma^2_{Ra}, \sigma^2_{Dted}$, then, the error e, that is defined as the difference between the estimated terrain height using altimeter outputs and the calculated terrain height via DTED at the position $\boldsymbol{p}_{l,L}$ can be expressed as follows.

$$\begin{aligned} e &\triangleq \hat{h}_{Ter}(\boldsymbol{p}_{l,L}) - \mathcal{H}(\boldsymbol{p}_{l,L}) \\ &= \{h_{Bar}(\boldsymbol{p}) - h_{Ra}(\boldsymbol{p})\} - \mathcal{H}(\boldsymbol{p}_{l,L}) \\ &= \Delta_{Bar} - \Delta_{Ra} - \Delta_{Dted} \end{aligned} \tag{13}$$

Based on the statistical assumptions about the errors above, e would also be zero-mean Gaussian with variance σ^2_{vert} where

$$\sigma^2_{vert} = \sigma^2_{Bar} + \sigma^2_{Ra} + \sigma^2_{Dted} \tag{14}$$

We use the distribution of e to assign a score to the points within the region which corresponds a pre-determined percent of the horizontal position uncertainty of a hypothesis. We define a scoring function $f_{sc}\left(\bar{\boldsymbol{p}}_{l,L}; \sigma_{vert}, \hat{h}_{Ter}(\boldsymbol{p}(t))\right)$ to assign a score to an arbitrary position $\bar{\boldsymbol{p}}_{l,L}$. The score of the position is equivalent to the likelihood of calculating the terrain height $\mathcal{H}(\bar{\boldsymbol{p}}_{l,L})$ from DTED given that $\hat{h}_{Ter}(\boldsymbol{p}(t))$ is observed. This likelihood can be evaluated as given in (15) where $\hat{h}_{Ter}(\boldsymbol{p}(t))$ is abbreviated as $\hat{h}_{Ter}(t)$ for brevity indicating the estimated terrain height at time t when the platform is located at position $\boldsymbol{p}$.

$$\begin{aligned} f_{sc}(\bar{\boldsymbol{p}}_{l,L}; \sigma_{vert}, \hat{h}_{Ter}(t)) &\triangleq \mathcal{L}\left(\mathcal{H}(\bar{\boldsymbol{p}}_{l,L}) | \hat{h}_{Ter}(t)\right) \\ &= N\left(\mathcal{H}(\bar{\boldsymbol{p}}_{l,L}) - \hat{h}_{Ter}(t); 0, \sigma^2_{vert}\right) \\ &= exp\left(-0.5\frac{\left(\mathcal{H}(\bar{\boldsymbol{p}}_{l,L}) - \hat{h}_{Ter}(t)\right)^2}{\sigma^2_{vert}}\right) \end{aligned} \tag{15}$$

1) GRIDDING

In this part of the algorithm, our purpose is to generate approximately equally spaced 2D points that are located within p_c percent probability region of a hypothesis ξ. In (16), $O^{\xi}(d_g)$ corresponds to the set of points where the angular separation distance equals to d_g in both the north and east direction.

$$O^{\xi}(d_g) \triangleq \left\{ \hat{\boldsymbol{p}}^{\xi}_{l,L} - \begin{bmatrix} i \\ j \end{bmatrix} d_g \;\middle|\; i,j \in \mathbb{Z} \right\} \tag{16}$$

where $\mathbb{Z}$ is the set of integers, and $\hat{\boldsymbol{p}}^{\xi}_{l,L}$ is the estimated horizontal coordinate of hypothesis ξ. We define a *gridding* function G on a hypothesis set as given in (17).

$$\begin{aligned} G(\xi; p_c, d_g) \triangleq \Big\{ \boldsymbol{x} \big| (\boldsymbol{x} - \hat{\boldsymbol{p}}^{\xi}_{l,L})^T (P^{\xi}_{l,L})^{-1} (\boldsymbol{x} - \hat{\boldsymbol{p}}^{\xi}_{l,L}) < \chi^2_{p_c}, \\ \boldsymbol{x} \in O^{\xi}(d_g) \Big\} \end{aligned} \tag{17}$$

where p_c denotes the coverage probability and $\chi^2_{p_c}$ is the two degrees of freedom chi-square inverse cumulative distribution function evaluated at p_c.

Utilizing the horizontal position covariance matrix, $P^{\xi}_{l,L}$, $G(\xi; p_c, d_g)$, abbreviated as $G(\xi)$, generates equally spaced 2D points inside the area which p_c percent of the horizontal uncertainty region of the hypothesis ξ covers. We employ the function in (15) to score the points in $G(\xi; p_c, d_g)$. Then, we create a new set of points, $\Upsilon^{\xi}_1(\tau_s) \subseteq G(\xi)$, whose scores are greater than the threshold τ_s. Thus, any point $\boldsymbol{x} \in \Upsilon^{\xi}_1(\tau_s)$ at time t satisfies the following property.

$$f_{sc}\left(\boldsymbol{x}; \sigma_{vert}, \hat{h}_{Ter}(t)\right) > \tau_s \tag{18}$$

Furthermore, we assign $\Upsilon^{\xi}_0(\tau_s) = G(\xi) \setminus \Upsilon^{\xi}_1(\tau_s)$ to represent the set of points in $G(\xi)$ whose scores are lower than τ_s. To be more precise, we illustrate $\Upsilon^{\xi}_1(\tau_s)$, and $\Upsilon^{\xi}_0(\tau_s)$, abbreviated as Υ^{ξ}_1 and Υ^{ξ}_0, on the same plot in Fig. 2. In this example, the threshold τ_s is set to 0.01. As a result, Υ^{ξ}_1 contains elements from $G(\xi)$, where the terrain height, calculated using DTED, falls within the range of $\hat{h}_{Ter} - 3\sigma_{vert}$ to $\hat{h}_{Ter} + 3\sigma_{vert}$. In Fig. 2. the blue mark at the center of the circle indicates $\hat{\boldsymbol{p}}^{\xi}_{l,L}$ that is the latitude and longitude of the hypothesis ξ. The area enclosed by the blue dashed circle corresponds to the 99% uncertainty region in the horizontal position of ξ, where the errors in latitude and longitude are not correlated and have equal variances, resulting in a nearly circular shaped region. The red-colored points form Υ^{ξ}_1. These points are indicated as *Probable platform positions* since the difference between the calculated terrain heights of these points and the measured terrain height $\hat{h}_{Ter}$ lie in the $3\sigma_{\text{vert}}$ interval of e in (13). Thus, it is reasonable to think that the true position lies in the region formed by red-colored dots. But, on the contrary, the elements of Υ^{ξ}_0, the black-colored points, are regarded as *improbable positions* since the deviation between the calculated terrain height of these points and the measured terrain height $\hat{h}_{Ter}$ are outside the $3\sigma_{\text{vert}}$ interval of e in (13).

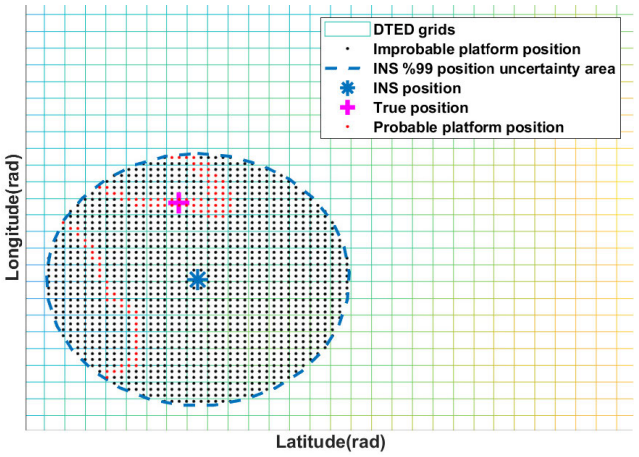

FIGURE 2. Demonstration of Υ_1^ξ and Υ_0^ξ.

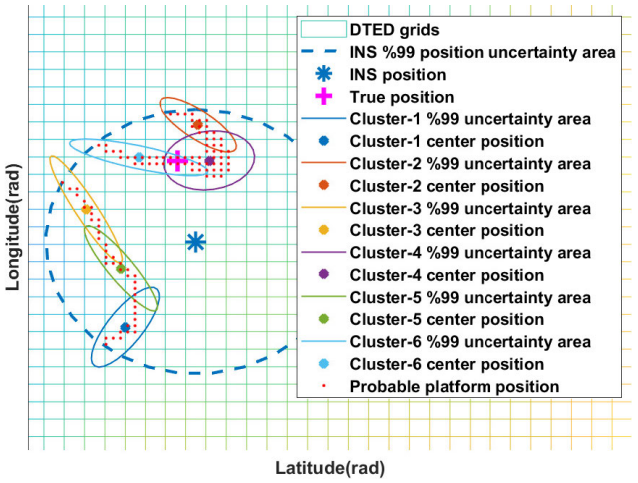

FIGURE 3. Demonstration of measurement set along with their uncertainty ellipses.

2) CLUSTERING

The cardinality of Υ_1^ξ gets larger as the position uncertainty of the hypothesis ξ increases. In addition to that, there could be many hypotheses due to terrain height similarities. Thus, constructing a fusion method that processes the elements of Υ_1^ξ separately may become computationally intractable. To overcome this issue, we model Υ_1^ξ as a Gaussian mixture (GM) by dividing it into smaller measurement sets and extracting each set's first and second central moment information. We utilize the well-known k-means clustering algorithm [41] to establish GM structure. In (19), A^ξ corresponds to the approximate area of the 99% horizontal position error uncertainty region of ξ in the horizontal geodetic coordinates.

$$A^\xi \triangleq \pi \left(1.5(\sigma_n^\xi + \sigma_e^\xi)\right)^2 \tag{19}$$

where σ_n^ξ and σ_e^ξ are the square roots of the diagonal terms of $P_{\mathrm{l,L}}^\xi$ corresponding to the standard deviations of the latitude and longitude errors of the hypothesis ξ. Let r_c and n_c denote, respectively, the minimum cluster radius in meters and the minimum number of members of a cluster. We set the number of clusters of the hypothesis ξ as given in (20).

$$K^\xi = max\left(\left\lfloor min\left(\frac{|\Upsilon_1^\xi|A^\xi}{|G(\xi)|}/\frac{\pi(3r_c)^2}{r_e^2}, \frac{|\Upsilon_1^\xi|}{n_c}\right)\right\rfloor, 1\right) \tag{20}$$

where $|\cdot|$ returns the cardinality of a set and $r_e \approx 6.4e6$ is the mean radius of the world curvature at latitude $\pi/4$. The explanation of the formulation in (20) is as follows. First, $max(\cdot)$ function on the right-hand side ensures that K^ξ would be at least one. The first entry of the $min(\cdot)$ function represents the ratio of the area covered by the elements of Υ_1^ξ to the area of a circle with the radius $3r_c$ meters scaled by r_e^2. The second entry in $min(\cdot)$ function represents the number of clusters if each cluster has n_c members. The $\lfloor\cdot\rfloor$ operator returns the greatest integer below the output of $min(\cdot)$ function. The purpose of the formulation in (20) is to establish a relationship between the number of clusters, spatial size and cardinality of the set Υ_1^ξ. The clustering step produces K^ξ number of sets $\theta_i \subseteq \Upsilon_1^\xi$ where $i \in \{1, 2, \ldots, K^\xi\}$. At this point, we create K^ξ measurements whose values and covariance matrices are obtained by (21) and (22);

$$z_i^\xi = \frac{\sum_{k=1}^{|\theta_i|} \theta_i(k) s_{\theta_i(k)}}{\sum_{k=1}^{|\theta_i|} s_{\theta_i(k)}} \tag{21}$$

$$R_i^\xi = \frac{1}{|\theta_i| - 1} \sum_{k=1}^{|\theta_i|} [\theta_i(k) - z_i^\xi][\theta_i(k) - z_i^\xi]^T \tag{22}$$

where $\theta_i(k)$ and $s_{\theta_i(k)}$ are k$^{\text{th}}$ member's 2D position and k$^{\text{th}}$ member's score of the measurement set θ_i. Continuing the example depicted in Fig.2, six measurements are generated from the set Υ_1^ξ. In Fig.3, cluster centers correspond to the measurements z^ξs, and the enclosing ellipses represent the 99% uncertainty regions derived from the covariance matrices R^ξs.

D. HYPOTHESIS SET CORRECTION

Hypothesis set correction is performed just after measurement generation step. Let $\Gamma(t_{Ra(k)})$ denote the set of tuples consisting of measurements and measurement covariances that are generated from all hypotheses at the time $t_{Ra(k)}$ as the following

$$\Gamma(t_{Ra(k)}) = \left\{(z_i^\xi, R_i^\xi) | i \in \{1, ., K^\xi\}, for\ all\ \xi \in \Xi^-(t_{Ra(k)})\right\} \tag{23}$$

Once the set $\Gamma(t_{Ra(k)})$ is generated, a new hypothesis set, $\Xi^+(t_{Ra(k)})$, is formed by fusing the hypotheses in $\Xi^-(t_{Ra(k)})$ with the appropriate members of $\Gamma(t_{Ra(k)})$. During this process, the cardinality of the hypothesis set may change$\left(|\Xi^-(t_{Ra(k)})| \neq |\Xi^+(t_{Ra(k)})|\right)$. The measurement-to-hypothesis association rule is provided in (24). The rationale for using this association rule is to prevent the exponential

Algorithm 2 Hypothesis Set Correction

Input: $\Omega(t_{Ra(k)})$
Output: $\Xi^{+}\left(t_{Ra(k)}\right)$

1: $\Xi^{+}\left(t_{Ra(k)}\right) = \emptyset$
2: **for** for each $(\xi, \gamma) \in \Omega(t_{R(k)})$ **do**
3: $\delta z = \hat{\boldsymbol{p}}_{l,L}^{\xi} - z^{\gamma}$
4: $K_{\text{gain}} = P^{\xi} H^{T} (H P^{\xi} H^{T} + R^{\gamma})^{-1}$
5: $\delta\hat{\boldsymbol{X}}^{\xi^{+}} = \delta\hat{\boldsymbol{X}}^{\xi} + K_{\text{gain}}(\delta z - H\delta\hat{\boldsymbol{X}}^{\xi})$
6: $P^{\xi^{+}} = (I - K_{\text{gain}} H) P^{\xi}$
7: $\hat{\boldsymbol{p}}_{l,L}^{\xi^{+}} = \hat{\boldsymbol{p}}_{l,L}^{\xi} - \delta\hat{\boldsymbol{X}}_{l,L}^{\xi^{+}}$
8: $\hat{\boldsymbol{v}}_{N,E}^{\xi^{+}} = \hat{\boldsymbol{v}}_{N,E}^{\xi} - \delta\hat{\boldsymbol{X}}_{v_N, v_E}^{\xi^{+}}$
9: $\hat{C}_{\text{NB}}^{\xi^{+}} = \left(I_{3\times 3} - S(\delta\hat{\boldsymbol{X}}_{r,p,y}^{\xi^{+}})\right)^{-1} \hat{C}_{\text{NB}}^{\xi}$
10: $\hat{\boldsymbol{f}}_{\text{bias}}^{\xi^{+}} = \hat{\boldsymbol{f}}_{\text{bias}}^{\xi} + \delta\hat{\boldsymbol{X}}_{f_{\text{BR}}}^{\xi^{+}} + \delta\hat{\boldsymbol{X}}_{f_{\text{BI}}}^{\xi^{+}}$
11: $\hat{\boldsymbol{\omega}}_{\text{bias}}^{\xi^{+}} = \hat{\boldsymbol{\omega}}_{\text{bias}}^{\xi} + \delta\hat{\boldsymbol{X}}_{\omega_{\text{BR}}}^{\xi^{+}} + \delta\hat{\boldsymbol{X}}_{\omega_{\text{BI}}}^{\xi^{+}}$
12: $\hat{M^{-1}}_{\text{acc}}^{\xi^{+}} = \left(I_{3\times 3} - DS(\delta\hat{\boldsymbol{X}}_{a_{\text{SF}}}^{\xi^{+}}, \delta\hat{\boldsymbol{X}}_{a_{\text{MA}}}^{\xi^{+}})\right) \hat{M^{-1}}_{\text{acc}}^{\xi^{+}}$
13: $\hat{M^{-1}}_{\text{gyr}}^{\xi^{+}} = \left(I_{3\times 3} - DS(\delta\hat{\boldsymbol{X}}_{g_{\text{SF}}}^{\xi^{+}}, \delta\hat{\boldsymbol{X}}_{g_{\text{MA}}}^{\xi^{+}})\right) \hat{M^{-1}}_{\text{gyr}}^{\xi^{+}}$
14: set $\delta\hat{\boldsymbol{X}}^{\xi^{+}} = \boldsymbol{0}$
15: append ξ^{+} into $\Xi^{+}(t_{Ra(k)})$
16: **end for**

increase in the number of newly generated hypotheses.

$$\ell(\xi,\gamma) = \begin{cases} 1 & (z^{\gamma} - \hat{\boldsymbol{p}}_{l,L}^{\xi})^{T} (P_{l,L}^{\xi})^{-1} (z^{\gamma} - \hat{\boldsymbol{p}}_{l,L}^{\xi}) < \chi^{2}_{0.99}, \\ & \xi \in \Xi^{-}, \gamma \in \Gamma \\ 0 & otherwise \end{cases} \tag{24}$$

Let $\Omega(t_{Ra(k)})$ denote the set of tuples consisting of hypothesis $\xi \in \Xi^{-}$, associated measurement $\gamma \in \Gamma$ as given in (25)

$$\Omega(t_{Ra(k)}) = \left\{(\xi,\gamma) | \xi \in \Xi^{-}(t_{Ra(k)}), \gamma \in \Gamma(t_{Ra(k)}), \ell(\xi,\gamma) = 1\right\} \tag{25}$$

Once the association set $\Omega(t_{Ra(k)})$ is formed, the closed-loop integration is performed for each ξ, γ pair in the set $\Omega(t_{Ra(k)})$. This integration procedure is given in Algorithm 2.

In Algorithm 2, ξ^{+} indicates the *corrected* hypothesis. In line 9, $\hat{C}_{\text{NB}}^{\xi}$ is the direction cosine matrix representation of the attitude of the hypothesis ξ. $DS(\cdot)$ forms a matrix where scale factor error estimates are located on diagonal indices and misalignment error estimates are located on off-diagonal indices as shown in (42), and $\left(\hat{M}^{-1}\right)^{\xi}$ is the inverse of (42) for the hypothesis ξ.

E. HYPOTHESIS PRUNING AND MERGING

The growing number of hypotheses is the primary computational burden of our method. Thus, eliminating the improbable hypotheses and merging similar hypotheses at each terrain aid cycle is necessary to ensure the algorithm's feasibility for real-time applications. In the merging process, which occurs immediately following the hypothesis set correction step, we utilize Cauchy-Schwarz (CS) divergence [42] to calculate dissimilarity scores between hypotheses. let $D[i,j]$ and t_m denote, respectively, the CS divergence between hypotheses i and j and merging threshold. We select CS divergence due to its symmetric and non-negativity properties ($D[i,j] = D[j,i]$ and $D[i,j] \geq 0$ for all i,j). The hypotheses i and j is merged if $D[i,j] < t_m$ where $D[i,j]$ is calculated as follows.

$$\begin{aligned} D[i,j] = {} & \frac{1}{4} log \left|\frac{\Sigma_i}{2}\right| + \frac{1}{2}\mu_i^{T}\Sigma_i^{-1}\mu_i + \frac{1}{4} log \left|\frac{\Sigma_j}{2}\right| \\ & + \frac{1}{2}\mu_j^{T}\Sigma_j^{-1}\mu_j + \frac{1}{2} log \left|\Sigma_j^{-1} + \Sigma_i^{-1}\right| \\ & - \frac{1}{2}\left(\Sigma_i^{-1}\mu_i + \Sigma_j^{-1}\mu_j\right)^{T} \cdot (\Sigma_i^{-1} + \Sigma_j^{-1})^{-1} \\ & \cdot \left(\Sigma_i^{-1}\mu_i + \Sigma_j^{-1}\mu_j\right) \end{aligned} \tag{26}$$

In (26), $|\cdot|$ is the determinant operator, Σ is the covariance matrix of the PVA part of the hypothesis, and μ is the PVA value of the hypothesis. If two or more hypotheses are to be merged, the mean and covariance of the merged hypothesis are obtained using Salmond's mixture merging structure [43]. The mean and covariance of the merged hypothesis as stated in (27), (28) are calculated for all navigation properties assuming that the weights of the hypotheses, w_k, equals to $\frac{1}{N}$ for all k.

$$\boldsymbol{\mu}_{merged} = \sum_{k=1}^{N} w_k \boldsymbol{\mu}_k \tag{27}$$

$$P_{merged} = \sum_{k=1}^{N} w_k \left[P_k + (\boldsymbol{\mu}_k - \boldsymbol{\mu}_{merged})(\boldsymbol{\mu}_k - \boldsymbol{\mu}_{merged})^{T}\right] \tag{28}$$

In Fig. 4, we compare the initial set of hypotheses, consisting of six individual hypotheses, with the reduced set of hypotheses achieved through the merging process. The

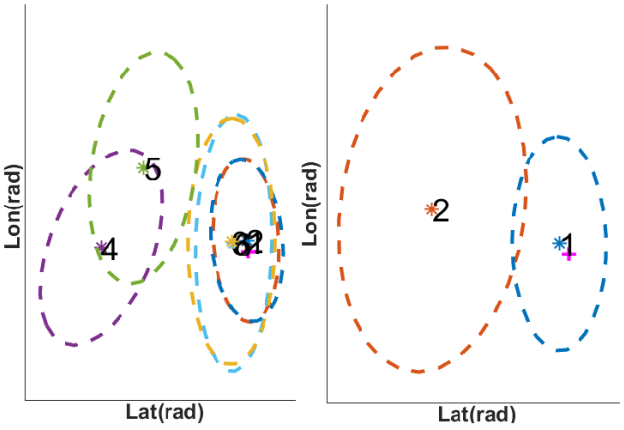

FIGURE 4. Two-dimensional illustration of merging, showing the gridding regions of hypotheses before and after the merge with a CS threshold of 2.

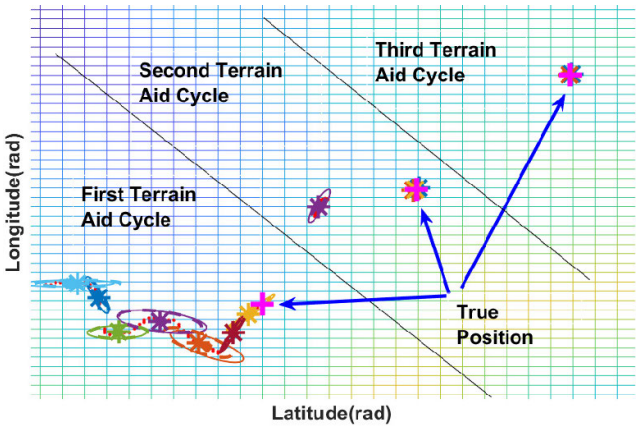

FIGURE 5. The demonstration of hypothesis merging/pruning.

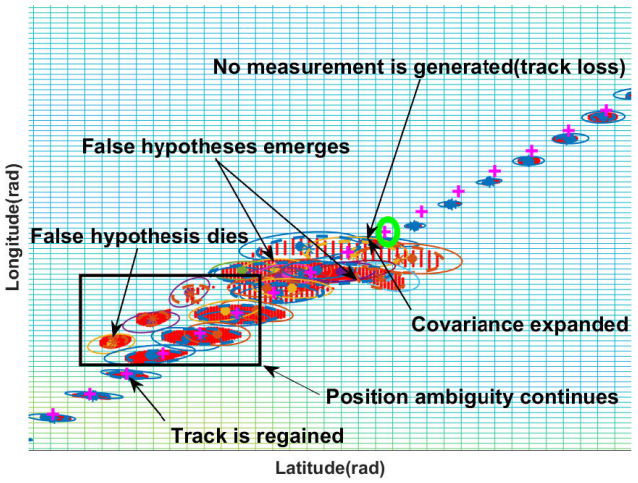

FIGURE 6. The effect of covariance expansion.

pairs of hypotheses whose divergence is less than two being merged. The merging process is illustrated by showing the initial set of hypotheses on the left, and the merged set of hypotheses on the right. Hypotheses 4 and 5 are merged to form hypothesis 2, while hypotheses 1, 2, 3, and 6 are merged to form hypothesis 1.

In the pruning process, which occurs at the onset of the hypothesis correction step, we assign a binary variable $\alpha^{\xi}(t_{Ra(k)}) \in \{0(discarded),\ 1(kept)\}$ that denotes the status of the hypothesis ξ. We set the value of the $\alpha^{\xi}(t_{Ra(k)})$ as given in (29).

$$\alpha^{\xi}(t_{Ra(k)}) = \begin{cases} 0 & if\ \ |\Upsilon_1^{\xi}| = 0\, and, |\Xi^{-}(t_{Ra(k)})| > 1 \\ 1 & otherwise \end{cases} \tag{29}$$

The first condition in (29) implies that ξ is discarded if all of its member locations obtained via gridding are improbable and there is at least one more hypothesis in $\Xi^{-}(t_{R(k)})$ other than ξ. Fig. 5 demonstrates a hypothesis pruning/merging example that takes place within three successive terrain aid cycles. The black lines separate hypothesis sets belonging to different time instances. For example, seven emerging hypotheses are located in different positions when the first hypothesis set correction occurs at time $t_{Ra(1)}$. These hypotheses are propagated until the second hypothesis set correction time $t_{Ra(2)}$. Just after the $t_{Ra(2)}$, hypotheses densify around two locations. The following hypothesis set correction at $t_{Ra(3)}$ resolves the two-position ambiguity, resulting in hypotheses to locate around the true platform position.

F. AD-HOC MEASURES TO PREVENT DIVERGENCE

Contrary to GNSS measurements that are independent of the INS solution, in our method, the generated position measurements are directly related to hypotheses. So, if the true platform position is outside the gridding area of all hypotheses, these hypotheses converge to the wrong place and eventually die. According to our observations, this situation occurs due to the following reasons. First, horizontal position error covariances of hypotheses converge to steady state values after a few correction steps. At that point, gridding regions of hypotheses slowly drift away from the true position in areas where terrain heights change gradually. Second, the error covariance propagation step stated in Algorithm 1 line 10 yields realistic error accumulation under small error assumptions [1]. Therefore, if the initial velocity and attitude errors are significant, their effect on the position error growth through the propagation equation does not reflect the actual error growth, which may cause the true position to reside outside all the hypotheses' gridding boundaries. To alleviate the divergence issue arising from these factors, we have suggested two ad-hoc methods: *covariance freezing* and *covariance expansion*. In covariance freezing, we manipulate the horizontal position error and horizontal velocity error covariances under certain circumstances. The position error covariance is manipulated such that the area of gridding region on the local level frame remain above the area of a circle with the radius r_{low} for every hypothesis ξ, while preserving the direction of the principal axes. Likewise, horizontal velocity error variances are set to v_{low}^2 if the drms value obtained from horizontal velocity error covariance is lower than the v_{low} parameter. In covariance expansion, we augment the position error covariances of all alive hypotheses by multiplying their eigenvalues with a scale factor s_{cof} in instances where no valid measurement can be obtained within the gridding regions of all alive hypotheses. In Algorithm-3 and 4, we share the details of our ad-hoc divergence prevention measures. In these algorithms, σ_n^{ξ} and σ_e^{ξ} are the square roots of the diagonal terms of horizontal position error covariance matrix $P_{\text{l,L}}^{\xi}$. e_1^{ξ} and e_2^{ξ} are the eigenvalues of $P_{\text{l,L}}^{\xi}$ and U^{ξ} and V^{ξ} are the left and right singular matrices of $P_{\text{l,L}}^{\xi}$. The value e_{max}^{ξ} equals $max(e_1^{\xi}, e_2^{\xi})$ and s_{cof}, r_{low} parameters are respectively uncertainty scale coefficient and approximate minimum position coverage radius in meters.

Fig. 6 demonstrates a case in which the true position of the platform is lost due to flying over a nearly flat region, and is regained after the covariance expansion procedure is

Algorithm 3 Covariance Freezing

Input: $\Xi^{+}(t_{Ra(k)})$, r_{low}, v_{low}
Output: $\Xi^{+}(t_{Ra(k)})$

```
for all ξ ∈ Ξ⁺(t_Ra(k)) do
    if (1.5(σ_n^ξ + σ_e^ξ) r_e)^2 < r_low^2 then
        κ = r_low^2 / (1.5(σ_n^ξ + σ_e^ξ) r_e)^2
        P_{l,L}^ξ ← U^ξ [ κ e_1^ξ   0
                          0   κ e_2^ξ ] V^{ξ T}
    end if
    if ( sqrt(P_{V_N}^ξ + P_{V_E}^ξ) ) < v_low then
        P_{V_N,V_E}^ξ ← [ v_low^2   0
                          0   v_low^2 ]
    end if
end for
return Ξ⁺(t_Ra(k))
```

Algorithm 4 Covariance Expansion

Input: $\Xi^{-}(t_{Ra(k)})$, s_{cof}
Output: $\Xi^{-}(t_{Ra(k)})$

```
while α^ξ(t_Ra(k)) = 0 for all ξ ∈ Ξ⁻(t_Ra(k)) do
    P_{l,L}^ξ ← s_cof [ e_max^ξ   0
                        0   e_max^ξ ]
end while
return Ξ⁻(t_Ra(k))
```

performed. In this case, the platform moves from the top right corner to the bottom left corner. The true position of the platform is represented by the purple-colored + symbol, while the red dots and ellipses denote the probable measurements obtained through the gridding process and hypothesis gridding regions, respectively. As the platform moves towards the position indicated by the bold green ellipse, measurements are obtained from the blue hypotheses even though it is drifting away from the true position. This phenomenon occurs because the terrain height under the platform is virtually identical to those present within the gridding region of the hypotheses. However, the estimated terrain height obtained by altimeter sensors deviates significantly from the calculated terrain heights within the gridding region of the hypothesis when the true position reaches the green-colored circle. As a consequence, no horizontal measurement is generated, and the track is lost unless supplementary measures are implemented. At that point, executing the covariance expansion algorithm increases the position error covariances of the viable hypotheses, thereby allowing for the generation of horizontal measurements as the true position falls within the expanded gridding region of the hypothesis. The covariance expansion can also lead to the formation of false hypotheses, as depicted in Fig. 6. However, these hypotheses disappear after a few correction cycles for this particular topography.

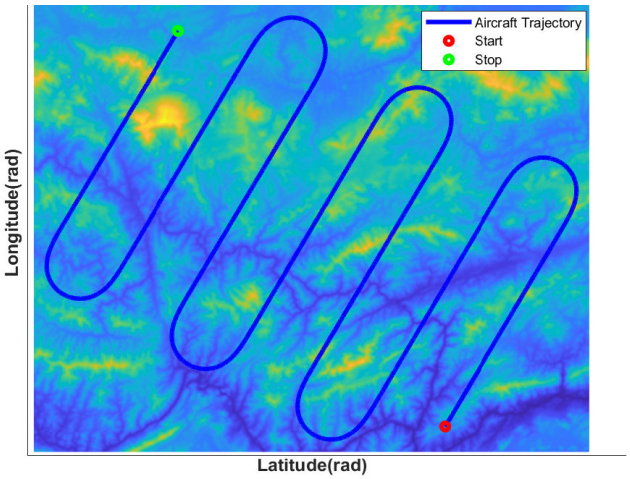

FIGURE 7. The bird's eye view of flight path.

G. HYBRID NAVIGATION OUTPUT

So far, we have focused on the generation and management of the multiple hypothesis sets. However, a single navigation PVA output and its covariance matrix are needed. The single PVA and its error covariance are calculated using (27) and (28) considering all alive hypotheses.

IV. SIMULATION RESULTS

To test our TAN method, first, we generate a flight trajectory as illustrated in Fig.7, and its corresponding errorless IMU data. Then, using (40) and (41), we obtain distorted IMU measurements. The total flight duration is 36 minutes, and the trajectory profile consists of straight-level flights followed by 1.5 G coordinated turns. The aircraft flies with a constant 250 m/s speed, and the side-slip, angle of attack angles are ignored in the data generation. We use level-1 DTED whose limits are $17°11'19'' - 18°58'27''$ for latitude, $98°32'55'' - 99°41'40''$ for longitude.

In our simulation setup, we use mems-grade IMU error specifications to distort true IMU data. To test the proposed filter consistency, we utilized the offline Monte Carlo test [44], in which the normalized estimation error squared (NEES) value is evaluated for only the horizontal position states at each terrain aid cycle. We set the Monte Carlo number as 100. The standard deviation values of gyroscope error specifications are as follows: $7°/hr$ bias repeatability error, 400 ppm scale factor error, 0.5 mrad misalignment error, 0.3°/hr bias instability error, $0.15°/\sqrt{hr}$ angle random walk error. Similarly, the standard deviation values for the accelerometer error specifications are detailed as follows: 2 mg bias repeatability error, 200 ppm scale factor error, 0.5 mrad misalignment error, 0.04 mg bias instability error, 0.03 m/s/$\sqrt{hr}$ velocity random walk error. The overall error in the measured terrain height is assumed to be zero-mean Gaussian with a standard deviation of 15 meters. Standard deviation values of the initial position, velocity, and heading errors are 2km in both north and east directions, 10 m/s in

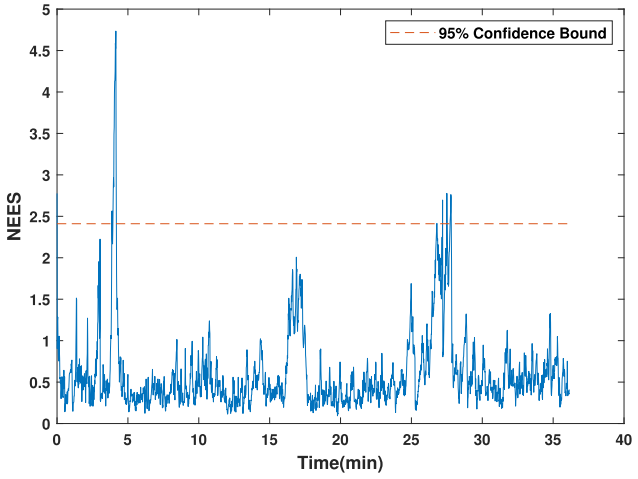

FIGURE 8. Horizontal position NEES for 100 Monte Carlo simulation.

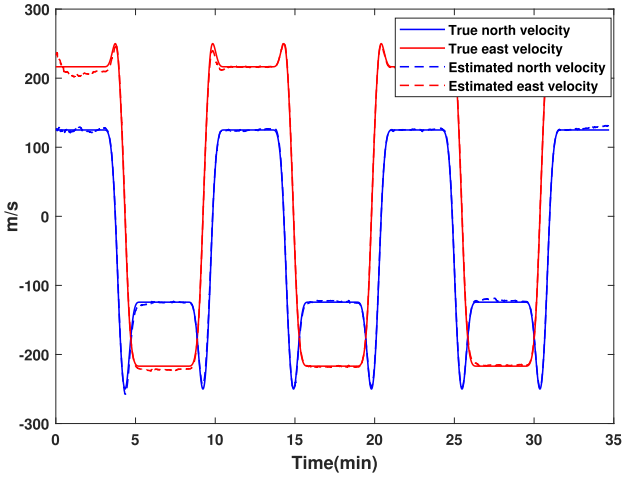

FIGURE 9. Single-run true velocity versus estimated velocity.

both north and east directions, and 200 mrad heading angle. The terrain aid cycle frequency is set to 0.5 Hz. The algorithm parameters, determined empirically, are specified as follows: $\tau_s = 0.01$, $r_c = r_{low} = 100$ meters, $n_c = 40$, $s_{cof} = 3$, and the hypothesis merging distance threshold is established at 1.8. We set the d_g parameter, which is unique for each hypothesis, as $d_g^{\xi} = 0.06(\sigma_n^{\xi} + \sigma_e^{\xi})r_e^{-1}$. The suitability of both TERCOM and SITAN is compromised in this scenario due to the substantial errors assumed in initial velocity and position. In Fig. 8, the NEES test statistic result is given. The dashed line illustrates the 95% confidence limit upper bound.

As the Fig. 8 demonstrates, apart from a few time indices, our filter is consistent as the calculated NEES is lower than 95% confidence bound, meaning that horizontal position errors are consistent with filter position covariance outputs. Considering all Monte Carlo runs, the mean of absolute northing and easting errors are lower than r_c parameter, which is 100 meters. Fig. 9 and Fig.10 show a comparison of the estimated horizontal velocity and heading angle with their respective true values. The error in the estimated east velocity decreases in the initial minutes of the flight. In contrast, the heading error remains relatively constant at approximately 120 mrad during straight flight and reduces to 15 mrad as the platform banks to maneuver. In Fig.11, the graph of the average number of hypotheses (ANH) of all Monte Carlo runs is depicted in two subplots. The plot on the top shows the ANH in the first 25 seconds, where ANH quickly rises to roughly 20 during the first few terrain aid cycles and then decreases due to the hypotheses pruning and merging process. The plot on the bottom indicates the ANH after the first minute, where ANH generally stays around one and slightly increases at some parts of the flight due to measurement ambiguities caused by topographical symmetries or flatness. This also indicates that the proposed method regulates the number of hypotheses without losing the true position during temporary ambiguities caused by topographical symmetries or flatness.

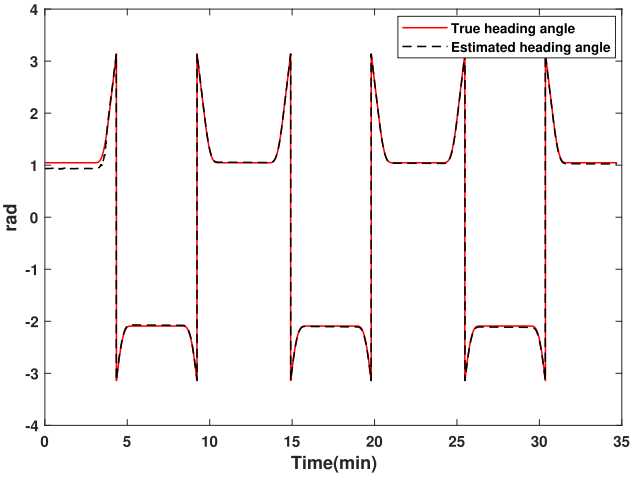

FIGURE 10. Single-run true heading versus estimated heading.

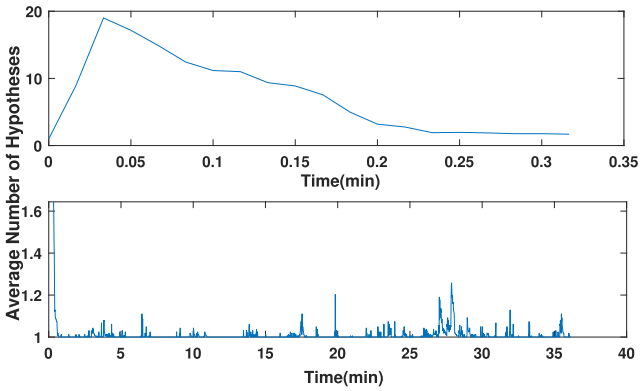

FIGURE 11. Average number of hypotheses in the first minute(top) and rest of the flight(bottom).

V. CONCLUSION AND FUTURE WORK

In this study, we proposed a novel multi-hypothesis based TAN method. We highlight the contributions of our study as

follows. In contrast to traditional TAN methods, the proposed multi-hypothesis approach demonstrates robustness to substantial initial errors in position, velocity, and heading. The number of hypotheses increases when the platform hovers over non-informative or repetitive terrain shapes and decreases when this ambiguous position situation is cleared. Thus, with the proper parameter selection, navigation continuity is maintained. Second, we employed an augmented error state that encapsulates both PVA errors and various IMU errors. This comprehensive state modeling reflects realistic position error growth in hypotheses resulting in converged position estimations even when low-end IMU measurements are used in simulations. The utilization of lower limit parameters for position and velocity error covariance, which we have implemented to prevent divergence, has the drawback that errors fluctuate around these parameters once the hypotheses have converged to the true position. We found that these covariance limit parameters can be decreased for more accurate radar/laser altimeters and terrains with distinctive features. In future studies, we will put effort into making these parameters adaptive to terrain profiles and the error model of distance-measuring altimeters. In the simulations, we made some assumptions for modeling simplifications. First, regardless of the aircraft's attitude, we assume that the distance measuring instrument is nadir pointing and measures the noise-corrupted vertical distance between terrain and aircraft. Additionally, we ignored any data latency issues and vertical channel dynamics, which play a critical role in real-time systems. In future work, we plan to extend our TAN method to account for these considerations.

APPENDIX A
BASICS OF INERTIAL NAVIGATION MATHEMATICS

A. REFERENCE FRAMES

A reference frame consists of a center point and three orthogonal right-handed axis sets. Throughout this paper, we utilize the NED navigation frame as the selected local level frame whose origin is the latitude, longitude, and altitude of the navigating platform's center, and its X, Y, and Z axes are aligned with the north, east, and local vertical, respectively. The other frame of reference we use is the body frame, whose origin is located at the center of the platform, and its X, Y, and Z axes are aligned with the platform roll, pitch, and yaw axes, respectively. In this study, we assume that body and geodetic frame origins are coincident. The IMU accelerometer $\boldsymbol{f}^B_{\mathrm{IB}}(t)$ and gyroscope $\boldsymbol{\omega}^B_{\mathrm{IB}}(t)$ outputs at time t are resolved in the body frame. The term *attitude* refers to the angular description between two frames. The direction cosine matrix (DCM) is the most used representation demonstrating the angular relationship between two frames.

In (30), C_{NB} is the DCM matrix that changes the resolution of a vector from body frame to navigation frame (e.g. $\boldsymbol{V}^N = C_{\mathrm{NB}}\boldsymbol{V}^B$). The functions $c(.)$ and $s(.)$ are cosine and sine functions, r, p, and y are the roll, pitch, and yaw angles between two frames.

$$C_{\mathrm{NB}} = \begin{bmatrix} c(y) & -s(y) & 0 \\ s(y) & c(y) & 0 \\ 0 & 0 & 1 \end{bmatrix} \cdot \begin{bmatrix} c(p) & 0 & s(p) \\ 1 & 1 & 0 \\ -s(p) & 0 & c(p) \end{bmatrix} \cdot \begin{bmatrix} 1 & 0 & 0 \\ 0 & c(r) & -s(r) \\ 0 & s(r) & c(r) \end{bmatrix} \tag{30}$$

B. CONTINUOUS-TIME MECHANIZATION EQUATIONS

The rate of change of latitude, longitude, and altitude with respect to time are given respectively in (31-33) as stated in [1].

$$\dot{l} = \frac{v_n}{(R_n + h)} \tag{31}$$

$$\dot{L} = \frac{v_e}{(R_e + h)cos(l)} \tag{32}$$

$$\dot{h} = -v_d \tag{33}$$

In the equations above, v_n, v_e, and v_d are north, east, and down velocities. R_n and R_e are meridian and traverse radius of curvature which are calculated as follows:

$$R_n = \frac{R(1 - e^2)}{(1 - e^2 sin^2(l))^{3/2}} \tag{34}$$

$$R_e = \frac{R}{(1 - e^2 sin^2(l))^{1/2}} \tag{35}$$

where R is the semi-major axis length and e is the major eccentricity of the ellipsoid. The rate of change of velocity expressed in the navigation frame is given in (36)

$$\dot{\boldsymbol{v}}^N = C_{\mathrm{NB}}\boldsymbol{f}^B - \left[2\boldsymbol{\omega}^N_{\mathrm{IE}} + \boldsymbol{\omega}^N_{\mathrm{EN}}\right] \times \boldsymbol{v}^N + \boldsymbol{g}^N \tag{36}$$

where $\boldsymbol{f}^B$ is the specific force vector sensed by the accelerometer triad, $\boldsymbol{g}^N$ is the plumb-bob gravity vector, $\boldsymbol{\omega}^N_{\mathrm{IE}}$ and $\boldsymbol{\omega}^N_{\mathrm{EN}}$ are respectively the rotation of the earth frame with respect to the inertial frame and rotation of the navigation frame with respect to the earth frame. These rotations can be calculated as follows:

$$\boldsymbol{\omega}^N_{\mathrm{IE}} = [\Omega_{\mathrm{earth}} cos(l),\ 0,\ -\Omega_{\mathrm{earth}} sin(l)]^T \tag{37}$$

$$\boldsymbol{\omega}^N_{\mathrm{EN}} = \left[\frac{v_e}{R_e + h},\ -\frac{v_n}{R_n + h},\ -\frac{v_e tan(l)}{R_e + h}\right]^T \tag{38}$$

Lastly, the attitude dynamics equation is given in (39)

$$\dot{C}_{\mathrm{NB}} = C_{\mathrm{NB}} S(\boldsymbol{\omega}^B_{\mathrm{IB}}) - S(\boldsymbol{\omega}^N_{\mathrm{IN}}) C_{\mathrm{NB}} \tag{39}$$

where $S(\cdot)$ converts the argument vector into the skew-symmetric matrix and $\boldsymbol{\omega}^N_{\mathrm{IN}} = \boldsymbol{\omega}^N_{\mathrm{IE}} + \boldsymbol{\omega}^N_{\mathrm{EN}}$.

C. IMU ERROR MODELLING

In equations (40) and (41), mathematical expressions of the measured accelerometer ($\tilde{\boldsymbol{f}}^B$) and gyroscope ($\tilde{\boldsymbol{\omega}}^B$) values are given as stated in [29].

$$\tilde{\boldsymbol{f}}^B = (I + M_a)\boldsymbol{f}^B + \delta\boldsymbol{f}_{\mathrm{BR}} + \delta\boldsymbol{f}_{\mathrm{BI}} + \delta\boldsymbol{f}_{\mathrm{VRW}} \tag{40}$$

$$\tilde{\boldsymbol{\omega}}^B = (I + M_g)\boldsymbol{\omega}^B + \delta\boldsymbol{\omega}_{\mathrm{BR}} + \delta\boldsymbol{\omega}_{\mathrm{BI}} + \delta\boldsymbol{\omega}_{\mathrm{ARW}} \tag{41}$$

In the above equations, the left-hand sides are the measured quantities. I is the 3×3 identity matrix, the lower script BR, BI indicate bias repeatability error ($^\circ/\sqrt{hr}$ for gyro, $mg/\sqrt{Hz}$ for accelerometer, respectively), and bias instability error ($^\circ/hr$ for gyro, mg for accelerometer, respectively) for the corresponding quantity, M_a and M_g are the 3×3 matrices consisting of misalignments errors (off-diagonal) and scale factor (diagonal) errors as shown in (42).

$$M_a = \begin{bmatrix} \delta f_{SF_x} & \delta f_{MA_{xy}} & \delta f_{MA_{xz}} \\ \delta f_{MA_{yx}} & \delta f_{SF_y} & \delta f_{MA_{yz}} \\ \delta f_{MA_{zx}} & \delta f_{MA_{zy}} & \delta f_{SF_z} \end{bmatrix} \tag{42}$$

$\delta \boldsymbol{f}_{\text{VRW}}$ and $\delta \boldsymbol{\omega}_{\text{ARW}}$ are random walk errors on velocity and angle, respectively. Repeatability, scale factor, and misalignment errors are considered as random constants. Therefore, their values are randomly selected based on their σ values for each Monte Carlo run and remain fixed. The implementation details of stochastic errors are not discussed here, but more information can be found in [24].

D. INS ERROR DYNAMICS

Error state propagation equation for the augmented state defined in (1) is given in (43). The explicit expression of the upper left 9×9 chunk is not discussed here, but it can be found in [1], [29], and [34].

$$\delta \dot{\boldsymbol{X}} = \begin{bmatrix} F^{\psi\psi}_{3\times3} & F^{\psi v}_{3\times3} & F^{\psi p}_{3\times3} & F^{\psi g}_{3\times15} & \mathbf{0} \\ F^{v\psi}_{3\times3} & F^{vv}_{3\times3} & F^{vp}_{3\times3} & \mathbf{0} & F^{va}_{3\times15} \\ F^{p\psi}_{3\times3} & F^{pv}_{3\times3} & F^{pp}_{3\times3} & \mathbf{0} & \mathbf{0} \\ \mathbf{0} & \mathbf{0} & \mathbf{0} & F^{gg}_{15\times15} & \mathbf{0} \\ \mathbf{0} & \mathbf{0} & \mathbf{0} & \mathbf{0} & F^{aa}_{15\times15} \end{bmatrix}_{39\times39} \delta \boldsymbol{X} + G_{39\times12} \left[\boldsymbol{n}_g^T \ \boldsymbol{n}_a^T \ \boldsymbol{b}_g^T \ \boldsymbol{b}_a^T \right]^T_{12\times1} \tag{43}$$

The rest of the sub-matrices in (43) are given in (44) and (45) and their derivations can be found in [31].

$$F^{\psi g}_{3\times15} = \left[-C_{\text{NB}} d(\boldsymbol{\omega}^B_{\text{IB}}) \ -C_{\text{NB}} Y_g \ -C_{\text{NB}} \ -C_{\text{NB}} \right] \tag{44}$$

$$F^{va}_{3\times15} = \left[C_{\text{NB}} d(\boldsymbol{f}^B_{\text{IB}}) \ C_{\text{NB}} Y_a \ C_{\text{NB}} \ C_{\text{NB}} \right] \tag{45}$$

where;

$$Y_g = \begin{bmatrix} -\omega^B_{\text{IB}_y} & \omega^B_{\text{IB}_z} & 0 & 0 & 0 & 0 \\ 0 & 0 & \omega^B_{\text{IB}_x} & -\omega^B_{\text{IB}_z} & 0 & 0 \\ 0 & 0 & 0 & 0 & -\omega^B_{\text{IB}_x} & \omega^B_{\text{IB}_y} \end{bmatrix} \tag{46}$$

Y_a is the specific force counterpart of Y_g, where $\boldsymbol{\omega}^B_{\text{IB}}$ is replaced by $\boldsymbol{f}^B_{\text{IB}}$. $F^{gg}_{15\times15}$ is a zero matrix except $F^{gg}[13, 13] = F^{gg}[14, 14] = F^{gg}[15, 15] = -\frac{1}{T_g}$. Similarly, $F^{aa}[13, 13] = F^{aa}[14, 14] = F^{aa}[15, 15] = -\frac{1}{T_a}$ where T_g and T_a are correlation time of bias instability of accelerometer and gyroscope. G is the noise gain matrix whose elements are zero except for $G[1:3, 1:3] = -C_{\text{NB}}$, $G[4:6, 4:6] = C_{\text{NB}}$, $G[22:24, 7:9] = I$, $G[36:39, 10:12] = I$. $\boldsymbol{n}_g$ and $\boldsymbol{n}_a$ are Gaussian white noise processes with the PSD N_g^2 for gyroscope, N_a^2 for accelerometer. $\boldsymbol{b}_a$ and $\boldsymbol{b}_g$ represent the bias instability terms which are usually modeled as a first-order Gauss-Markov process [24], [29]. To calculate the error state propagation in a computer, (43) is needed to be discretized. We employ Van-Loan's method [40] to obtain discrete counterparts of $F(t)$ and $Q(t)$ as the following equations.

$$A = \begin{bmatrix} -F & GWG^T \\ \mathbf{0} & F^T \end{bmatrix} \Delta t \tag{47}$$

$$B = e^A = \begin{bmatrix} \cdots & \Phi^{-1} Q_d \\ \mathbf{0} & \Phi^T \end{bmatrix} \tag{48}$$

REFERENCES

[1] D. Titterton, J. Weston, and J. Weston, *Strapdown Inertial Navigation Technology* (IEE Radar, Sonar, Navigation and Avionics Series). Reston, VA, USA: American Institute of Aeronautics and Astronautics, 2004.

[2] M. S. Grewal, L. R. Weill, and A. P. Andrews, *Global Positioning Systems, Inertial Navigation, and Integration*. New York, NY, USA: Wiley, 2001.

[3] J. P. Golden, "Terrain contour matching (TERCOM): A cruise missile guidance aid," in *Image Processing for Missile Guidance*, vol. 238. Bellingham, WA, USA: SPIE, Dec. 1980, pp. 10–18. [Online]. Available: https://www.spiedigitallibrary.org/conference-proceedings-of-spie/0238/0000/Terrain-Contour-Matching-TERCOM-A-Cruise-Missile-Guidance-Aid/10.1117/12.959127.full

[4] W. Baker and R. Clem, "Terrain contour matching [TERCOM] primer," Aeronautical Syst. Division, Wright-Patterson AFB, Wright-Patterson Air Force Base, OH, USA, Tech. Rep. ASP-TR-77-61, 1977.

[5] J. Hollowell. (Jan. 1990). *Heli/SITAN: A Terrain Referenced Navigation Algorithm for Helicopters*. [Online]. Available: https://www.osti.gov/biblio/5127167

[6] L. Zhao, N. Gao, B. Huang, Q. Wang, and J. Zhou, "A novel terrain-aided navigation algorithm combined with the TERCOM algorithm and particle filter," *IEEE Sensors J.*, vol. 15, no. 2, pp. 1124–1131, Feb. 2015.

[7] T. Sonmez and H. E. Bingol, "Modeling and simulation of a terrain aided inertial navigation algorithm for land vehicles," in *Proc. IEEE/ION Position, Location Navigat. Symp.*, May 2008, pp. 1046–1052. [Online]. Available: http://ieeexplore.ieee.org/document/4570078/

[8] F. Qingtang, S. Lincheng, and C. Wenseng, "Terrain aided navigation using PDAF," in *Proc. IEEE Int. Conf. Robot., Intell. Syst. Signal Process.*, Oct. 2003, pp. 1063–1068.

[9] P. Ding and X. Cheng, "A new contour-based combined matching algorithm for underwater terrain-aided strapdown inertial navigation system," *Measurement*, vol. 202, Oct. 2022, Art. no. 111870. [Online]. Available: https://www.sciencedirect.com/science/article/pii/S0263224122010673

[10] E. Wei, C. Dong, Y. Yang, S. Tang, J. Liu, G. Gong, and Z. Deng, "A robust solution of integrated SITAN with TERCOM algorithm: Weight-reducing iteration technique for underwater Vehicles' gravity-aided inertial navigation system," *Navigation*, vol. 64, no. 1, pp. 111–122, Mar. 2017.

[11] H. Ze Peng, Y. Jun, W. Wen Wei, and M. B. Zhi, "An algorithm of terrain matching aided navigation for UAVs," in *Proc. IEEE CSAA Guid., Navigat. Control Conf. (CGNCC)*, Aug. 2018, pp. 1–6.

[12] M. Cowie, N. Wilkinson, and R. Powlesland, "Latest development of the TERPROM digital terrain system (DTS)," in *Proc. IEEE/ION Position, Location Navigat. Symp.*, May 2008, pp. 1219–1229.

[13] G. Yuan, H. Zhang, K. Yuan, and L. Zhu, "Improved SITAN algorithm in the application of aided inertial navigation," in *Proc. Int. Conf. Meas., Inf. Control*, vol. 2, May 2012, pp. 922–926.

[14] R. Enns and D. Morrell, "Terrain-aided navigation using the Viterbi algorithm," *J. Guid., Control, Dyn.*, vol. 18, no. 6, pp. 1444–1449, Nov. 1995, doi: 10.2514/3.21566.

[15] N. Bergman, L. Ljung, and F. Gustafsson, "Terrain navigation using Bayesian statistics," *IEEE Control Syst.*, vol. 19, no. 3, pp. 33–40, Jun. 1999.

[16] N. Bergman, "A Bayesian approach to terrain-aided navigation," *IFAC Proc. Volumes*, vol. 30, no. 11, pp. 1457–1462, Jul. 1997.

[17] F. Gustafsson, F. Gunnarsson, N. Bergman, U. Forssell, J. Jansson, R. Karlsson, and P.-J. Nordlund, "Particle filters for positioning, navigation, and tracking," *IEEE Trans. Signal Process.*, vol. 50, no. 2, pp. 425–437, Feb. 2002.

[18] B. Turan and A. T. Kutay, "Particle filter studies on terrain referenced navigation," in *Proc. IEEE/ION Position, Location Navigat. Symp. (PLANS)*, Apr. 2016, pp. 949–954.

[19] C. Palmier, K. Dahia, N. Merlinge, P. Del Moral, D. Laneuville, and C. Musso, "Adaptive approximate Bayesian computational particle filters for underwater terrain aided navigation," in *Proc. 22th Int. Conf. Inf. Fusion (FUSION)*, Jul. 2019, pp. 1–8.
[20] G. Salavasidis, A. Munafò, S. D. McPhail, C. A. Harris, D. Fenucci, M. Pebody, E. Rogers, and A. B. Phillips, "Terrain-aided navigation with coarse maps—Toward an Arctic crossing with an AUV," *IEEE J. Ocean. Eng.*, vol. 46, no. 4, pp. 1192–1212, Oct. 2021.
[21] F. C. Teixeira, A. Pascoal, and P. Maurya, "A novel particle filter formulation with application to terrain-aided navigation," *IFAC Proc. Volumes*, vol. 45, no. 5, pp. 132–139, 2012.
[22] W. Rupeng, L. Ye, M. Teng, C. Zheng, G. Yusen, and X. Pengfei, "Improvements to terrain aided navigation accuracy in deep-sea space by high precision particle filter initialization," *IEEE Access*, vol. 8, pp. 13029–13042, 2020.
[23] B. Turan, "Comparison of nonlinear filtering methods for terrain referenced aircraft navigation," in *Proc. IEEE/ION Position, Location Navigat. Symp. (PLANS)*, Apr. 2020, pp. 144–149.
[24] J. A. Farrell, F. O. Silva, F. Rahman, and J. Wendel, "Inertial measurement unit error modeling tutorial: Inertial navigation system state estimation with real-time sensor calibration," *IEEE Control Syst. Mag.*, vol. 42, no. 6, pp. 40–66, Dec. 2022.
[25] P.-J. Nordlund and F. Gustafsson, "Marginalized particle filter for accurate and reliable terrain-aided navigation," *IEEE Trans. Aerosp. Electron. Syst.*, vol. 45, no. 4, pp. 1385–1399, Oct. 2009.
[26] B. Ristic, S. Arulampalam, and N. Gordon, *Beyond Kalman Filter: Particle Filters for Tracking Applications*. Norwood, MA, USA: Artech House, 2003.
[27] C. Palmier, K. Dahia, N. Merlinge, D. Laneuville, and P. del Moral, "Interacting weighted ensemble Kalman filter applied to underwater terrain aided navigation," in *Proc. Amer. Control Conf. (ACC)*, May 2021, pp. 1541–1546.
[28] F. C. Teixeira, J. Quintas, P. Maurya, and A. Pascoal, "Robust particle filter formulations with application to terrain-aided navigation," *Int. J. Adapt. Control Signal Process.*, vol. 31, no. 4, pp. 608–651, Apr. 2017, doi: 10.1002/acs.2692.
[29] R. Rogers, *Applied Mathematics in Integrated Navigation Systems* (AIAA Education Series), no. 1. Reston, VA, USA: American Institute of Aeronautics and Astronautics, 2003.
[30] A. Noureldin, T. Karamat, and J. Georgy, *Fundamentals of Inertial Navigation, Satellite-based Positioning and their Integration*. Berlin, Germany: Springer, 2012.
[31] J. A. Farrell and M. Barth, *The Global Positioning System and Inertial Navigation: Theory and Practice*, vol. 370. New York, NY, USA: McGraw-Hill, 1999.
[32] Y. Yuksel, N. El-Sheimy, and A. Noureldin, "Error modeling and characterization of environmental effects for low cost inertial MEMS units," in *Proc. IEEE/ION Position, Location Navigat. Symp.*, May 2010, pp. 598–612.
[33] N. El-Sheimy, H. Hou, and X. Niu, "Analysis and modeling of inertial sensors using Allan variance," *IEEE Trans. Instrum. Meas.*, vol. 57, no. 1, pp. 140–149, Jan. 2008.
[34] P. Groves, *Principles of GNSS, Inertial, and Multisensor Integrated Navigation Systems*, 2nd ed. Norwood, MA, USA: Artech House, 2013.
[35] D. Goshen-Meskin and I. Y. Bar-Itzhack, "Observability analysis of piecewise constant systems. I. Theory," *IEEE Trans. Aerosp. Electron. Syst.*, vol. 28, no. 4, pp. 1056–1067, Oct. 1992.
[36] H. Yu, W. Wu, M. Wu, M. Yu, and M. Hao, "Stochastic observability-based analytic optimization of SINS multiposition alignment," *IEEE Trans. Aerosp. Electron. Syst.*, vol. 51, no. 3, pp. 2181–2192, Jul. 2015.
[37] G. Siouris, *Missile Guidance and Control Systems*. Cham, Switzerland: Springer, 2004.
[38] P. G. Savage, "Strapdown inertial navigation integration algorithm design—Part 1: Attitude algorithms," *J. Guid., Control, Dyn.*, vol. 21, no. 1, pp. 19–28, Jan. 1998, doi: 10.2514/2.4228.
[39] P. G. Savage, "Strapdown inertial navigation integration algorithm design Part 2: Velocity and position algorithms," *J. Guid., Control, Dyn.*, vol. 21, no. 2, pp. 208–221, 1998, doi: 10.2514/2.4242.
[40] C. Van Loan, "Computing integrals involving the matrix exponential," *IEEE Trans. Autom. Control*, vol. AC-23, no. 3, pp. 395–404, Jun. 1978.
[41] J. A. Hartigan and M. A. Wong, "Algorithm AS 136: A k-means clustering algorithm," *Appl. Statist.*, vol. 28, no. 1, pp. 100–108, Jan. 1979. [Online]. Available: http://www.jstor.org/stable/2346830
[42] F. Nielsen, K. Sun, and S. Marchand-Maillet, "On Hölder projective divergences," *Entropy*, vol. 19, no. 3, p. 122, Mar. 2017. [Online]. Available: http://www.mdpi.com/1099-4300/19/3/122
[43] D. J. Salmond, D. P. Atherton, and J. A. Bather, "Mixture reduction algorithms for uncertain tracking," *IFAC Proc. Volumes*, vol. 21, no. 9, pp. 775–780, Aug. 1988. [Online]. Available: https://www.sciencedirect.com/science/article/pii/S1474667017548223
[44] Y. Bar-Shalom, X. Li, and T. Kirubarajan, *Estimation With Applications to Tracking and Navigation: Theory Algorithms and Software*. Hoboken, NJ, USA: Wiley, 2004.

AYBARS TOKTA received the B.S. and M.S. degrees from Gebze Technical University, where he is currently pursuing the Ph.D. degree. He was a Research Assistant with Gebze Technical University, from 2015 to 2021. He is a Navigation System Design Engineer with Aselsan Inc. His current research interests include signal processing, target tracking, and navigation.

ALİ KÖKSAL HOCAOĞLU received the Ph.D. degree in electrical engineering from the University of Missouri, Columbia, USA, in 2000. From 2000 to 2003, he was a Postdoctoral Research Associate with the University of Missouri and the University of Florida, USA. From 2003 to 2012, he was the Chief Researcher with the Marmara Research Center, and the Informatics and Information Security Research Center, Scientific and Technological Research Council, Turkey. He is currently an Assistant Professor with the Department of Electronics Engineering, Gebze Technical University, Turkey. He has worked on a wide variety of applied research problems on automatic target recognition, with a focus on problems in pattern recognition, image and signal analysis, and sensor fusion. His current research interests include developing multi-sensor target detection and tracking systems for border surveillance using passive sensors.